MEASUREMENTS OF HEAT TRANSFER ON HEMISPHERES AT RAREFIED FLOW CONDITIONS USING LIQUID CRYSTALS

N. L. Donaldson[1], L. Doherty[2], Peter Ireland[3], and J. Merrifield[4]

[1] *Oxford Thermofluids Institute, Southwell Building, Osney Mead, Oxford, OX2 0ES, UK, Email (current): n.l.donaldson@soton.ac.uk*

[2] *Oxford Thermofluids Institute, Southwell Building, Osney Mead, Oxford, OX2 0ES, UK, Email: luke.doherty@eng.ox.ac.uk*

[3] *Oxford Thermofluids Institute, Southwell Building, Osney Mead, Oxford, OX2 0ES, UK, Email: peter.ireland@eng.ox.ac.uk*

[4] *Fluid Gravity Engineering, 1 West Street, Emsworth, Hampshire, UK, PO10 7DX, Email: jim.merrifield@fluidgravity.co.uk*

ABSTRACT

Experiments have been conducted in the Oxford Low Density Tunnel (LDT) to characterise the heat transfer distribution over hemisphere-capped cylinders at rarefied flow conditions using therochromic liquid crystals. Two hemisphere-cylinders measuring 10mm and 15mm in diameter were tested at conditions corresponding to Knudsen numbers of 0.02 and 0.1 and Mach numbers of 5.4 and 5.8, respectively. The hemisphere-cylinders were axially aligned with the flow, achieving an effective angle of attack of 0^o.

The results were post-processed using an in-house code developed at the Oxford Thermofluids Institute and distributions of heat transfer coefficient across the hemisphere surfaces extracted. These data were found to be of high resolution with stagnation heat transfer coefficients of 30.3 and 41.7 W/m^2K on the 10mm and 15mm probes at the $Kn = 0.1$ and $Kn = 0.02$ conditions, respectively. Comparisons with axisymmetric DSMC simulations were found to agree well, with maximum stagnation point errors of 4.5% and 5.3%, respectively.

Keywords: hypersonic wind tunnel; transient thermal analysis; space debris re-entry heating; DSMC.

1. INTRODUCTION

The study of space debris demise is an important area of scientific enquiry as the total population of tracked debris items has increased by several orders of magnitude since the advent of spaceflight. During atmospheric re-entry, the aerothermal environment to which debris items are subjected varies hugely, with a wide variety of physical phenomena taking precedence at different altitudes and velocities. One of the most important of these is the slip-transition regime, where freestream Knudsen numbers lie in the range $0.001 \leqslant Kn \leqslant 1.0$. This regime contributes significantly to the thermal pre-soak phenomenon, which is a major factor in the determination of the initial temperature of debris prior to the onset of peak heating in the continuum regime (where $Kn < 0.001$). It is typically this peak heating which determines whether or not a piece of debris will completely demise, and so an understanding of its initial conditions (and hence heating behaviour in the slip-transition regime) is equally important.

In this paper, a pair of transient thermal experiments on hemispheres performed using thermochromic liquid crystals are presented. This type of geometry was selected for three reasons:

1. Modern debris demise simulation codes utilise geometric primitives in order to calculate thermal fluxes and re-entry trajectories, the hemisphere-cylinder being a common analogue of a fuel tank.
2. Hemisphere-cylinders do not feature sharp edges or corners as in flat cylinders or cuboids, thereby allowing a one-dimensional heat transfer assumption to be applied during post-processing.
3. A hemisphere-cylinder positioned with its longitudinal axis parallel to a fluid flow may be numerically simulated using an axisymmetric formulation, hence allowing time-efficient validation of existing numerical tools.

The experiments were performed in the Low Density Tunnel (LDT), an experimental facility at the Oxford Thermofluids Institute (OTI) at the University of Oxford capable of producing hypersonic, slip-transition regime flows. This facility has previously in conjunction with thermochromic liquid been used to

[1] Currently a post-doctoral research assistant at the Department of Aeronautics and Astronautics, University of Southampton, University Road, Southampton, SO17 1BJ, UK

Section 2 describes the LDT itself, and specifies the test conditions utilised for the present work. Section 3 describes the set up of the transient thermal experiments and the manufacture of the hemisphere-capped cylindrical probes used. Transient thermal experiments using thermochromic liquid crystal are also described in this section, and the associated calibration procedure. Section 4 describes a series of DSMC simulations performed at the same conditions as the experiments, and Section 5 elaborates upon the liquid crystal post-processing technique used in the present work. Finally, the results of both experiments and simulations are presented in Section 6.

2. EXPERIMENTAL FACILITY

The experiments performed for the present work utilised the Oxford Low Density Tunnel (LDT), a vacuum wind tunnel capable of producing hypersonic rarefied flows for the study of aerothermodynamic phenomena. The facility is powered by a vapour diffusion booster pump, which is backed by a Roots type mechanical booster and three high vacuum rotary piston pumps, providing an ultimate pumping capacity of $\sim$ 22000 litres/sec. The LDT was first installed at the OTI in the early 1960s and has been used for a variety of studies examining the heat transfer to simple geometries in low density flows [11] [4] [7] [16]. A diagram showing the layout and major components of the facility is presented in Figure 1.

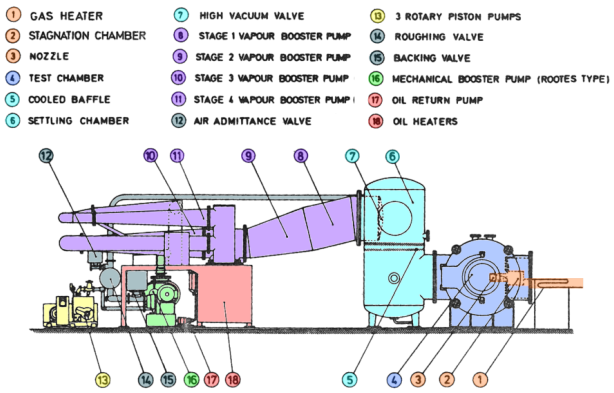

Figure 1. Diagram showing the layout and main components of the LDT

The LDT is capable of producing a hypersonic plume using its contoured nozzle with core Mach numbers in excess of 5 ($Ma \geqslant 5$), and Knudsen numbers well into the slip-transition regime ($0.001 \leqslant Kn \leqslant 1.0$). The facility's gas conditioning system may be supplied by the OTI's central dry compressed air system, or by a locally installed gas bottle. The system is also able to preheat the working gas up to $\sim$530 K using a combination of a heated stagnation chamber and inline heater connected to the inlet pipework. A digital mass flow controller has also been installed which allows mass flow rates up to 50 SLPM ($\sim$1 g/s at standard conditions) to be admitted to the gas conditioning system.

A summary of instrumentation installed in the LDT is presented in Table 1. The sensor model numbers, measurement ranges, measurement uncertainty (as stated by the manufacturers), and the flow variables they measure are listed.

As described in [5], the facility has recently undergone refurbishment and recommissioning. Two test conditions were used in the current work, which were characterised using a Pitot probe affixed to the LDT traversing mechanism. These conditions both used dry air from the centralised OTI compressor system as the working gas, and a setpoint of 385 K for the gas heaters in the LDT stagnation chamber. Inlet mass flow rate setpoints of 10 and 25 SLPM were used, and the location of the probe downstream of the nozzle exit was set to 108mm and 80mm, respectively, in order to achieve the desired level of rarefaction in the flow (see Section 2.1). CFD simulations of the test conditions were also performed in order to both aid in the calculation of the aforementioned probe positions, and to derive input variables for subsequent DSMC simulations.

2.1. Characterisation of test conditions

The capabilities of the LDT were characterised using the results of a Pitot survey of the test plume produced by the facility's contoured nozzle. These measurements were performed at six separate flow conditions, with inlet mass flow rates, w, of 5, 10, 15, 20, 25, and 30 SLPM, and total temperatures of 293 K and 385 K, totalling 12 separate flow conditions. Data from these surveys was subsequently used to identify flow conditions for the present work (in conjunction with CFD simulations).

For each flow survey, the LDT linear traversing mechanism was used to manoeuvre a cylindrical Pitot probe (with an outer diameter of 5mm and wall thickness of 0.5mm) to various positions within the nozzle plume, allowing it to take measurements at 10 mm increments along the nozzle centreline (referred to from here on as the nozzle x axis – see Figure 2). At each sampling location along the nozzle x axis, a radial survey was performed wherein the probe was translated perpendicular to this axis (referred to as the $y(r)$ axis in Figure 2) in 1 mm increments, culminating in a two dimensional survey of the plume. This particular sampling geometry was selected based upon the assumption that the nozzle flow would be axisymmetric, and thus invariant about the nozzle x axis.

A centring procedure for the traverse mechanism was devised in order to ensure that the Pitot probe would be accurately positioned relative to the true centreline of the nozzle flow. This procedure involved a Pitot survey performed over a grid of sampling locations in the $y - z$ plane at the nozzle exit, $x = 0$ (see Figure 2) near the assumed centre of the nozzle plume. The results of this survey were then interrogated using 2D linear interpolation. The point at which the highest interpolated Pitot

Measurement	Symbol	Sensor	Range	Accuracy
Mass flow rate	w	Omega FMA-2609A	$0 - 50\,SLPM$	$\pm 0.8\% + 0.2\%$ FSR
Stag. chamber pres.	p_0	MKS Baratron 122A	$0 - 13,300\,Pa$	$\pm 0.5\%$ FSR
Test chamber pres.	p_∞	Edwards Pirani APG100-XLC	$0.01 - 100,000\,Pa$	$\pm 15\%$ FSR @ $< 1000 Pa$
Test chamber pres.	p_∞	Inficon CDG025D	$0 - 133\,Pa$	$\pm 0.2\%$ FSR
Pitot pres.	p_T	First Sensor 144LP05D-PCB	$0 - 500\,Pa$ (diff.)	$\pm 2.5\%$ FSO
Stag. chamber temp.	T_0	Thermocouple (type K)	$3 - 987\,K$	$\max(\pm 2.2^oC, \pm 0.75\%)$
Test chamber temp.	T_∞	Thermocouple (type K)	$3 - 987\,K$	$\max(\pm 2.2^oC, \pm 0.75\%)$

Table 1. Summary of LDT test section instrumentation. Note that the abbreviations "stag.", "pres.", and "temp." are used in place of stagnation, pressure, and temperature, respectively. "FSR" and "FSO" refer, respectively, to the full scale measurement range and full scale voltage output of a given sensor. All sensors measured absolute values unless otherwise indicated with the abbreviation "diff." (differential).

pressure occurred was then set as the "true" centre coordinate for the traversing mechanism. The precision of the traverse stepper motors and position encoders allowed for these coordinates to be set to an accuracy of 0.01mm.

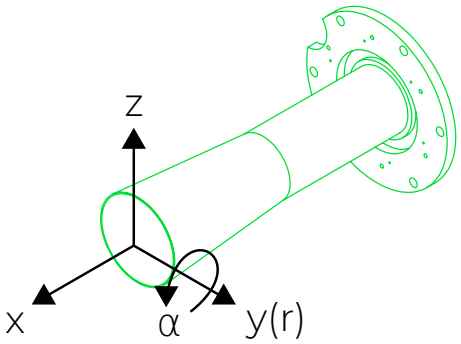

Figure 2. Diagram showing the coordinate system applied to the LDT nozzle. The positive x axis is coincident with the flow direction of the nozzle plume, and the origin of the coordinate system is taken to be the point at which the maximum Pitot pressure at the nozzle exit ($x = 0$) was found during the centring procedure. The y axis is referred to as the radial direction, r, in the present work. The angle of incidence of a test piece relative to the x axis is represented by the symbol α

A CFD simulation was also performed for each flow case and validated against the Pitot data in order to allow the interpolation of initial conditions for subsequent experimental studies, and provide input variables for DSMC simulations. This interpolation was deemed necessary as the static properties of the flow were not measured during the Pitot surveys.

The CFD simulations' boundary conditions were set using readings of pressure and temperature in the LDT stagnation chamber (total) and test chamber (static), as measured by the LDT's various housekeeping sensors during the characterisation surveys (see Table 1). Figure 3 shows the outline of the CFD geometry and the applied boundary conditions, and Table 2 shows the solver settings used. The calculations themselves were performed using ANSYS FLUENT on a structured grid comprising $\sim 500,000$ cells, wherein a standard no-slip wall formulation was applied to the nozzle geometry. Gas properties were modelled using piecewise polynomials fitted to NIST data for air at low pressures over a temperature range of $30\,K \leqslant T \leqslant 600\,K$ [6]. Good agreement was observed between simulated and experimental Pitot pressure values along the nozzle x axis at all tested conditions.

Setting/parameter	Value
FLUENT version	19.2
Energy equation	Enabled
Solver formulation	Density
Geometry formulation	Axisymmetric
Gas thermochemical model	Air, NIST derived
Numerical formulation	Implicit
Numerical scheme	AUSM
Nozzle wall formulation	No-slip
Nozzle wall temperature	$293\,K$
Turbulence model	None; laminar
Solution steering	On; hypersonic preset

Table 2. Parameters and settings of the CFD simulations performed for the present work.

$$Kn = \frac{\lambda}{L} = \frac{k_\mathrm{B} T}{\sqrt{2}\pi\sigma^2 p L} \tag{1}$$

The results of the CFD simulations were characterised by their respective Knudsen numbers (see Equation 1). This non-dimensional number is a measure of rarefaction in a fluid; the formulation used in the present work is based upon the kinetic theory of gasses. Here, λ is the mean free path (the mean distance a gas molecule will travel before colliding with another), k_B is Boltzmann's constant, T and p are the static temperature and pressure of the flow (respectively), σ is the mean diameter of a gas molecule (taken to be 4×10^{-10}m for air [10]), and L is

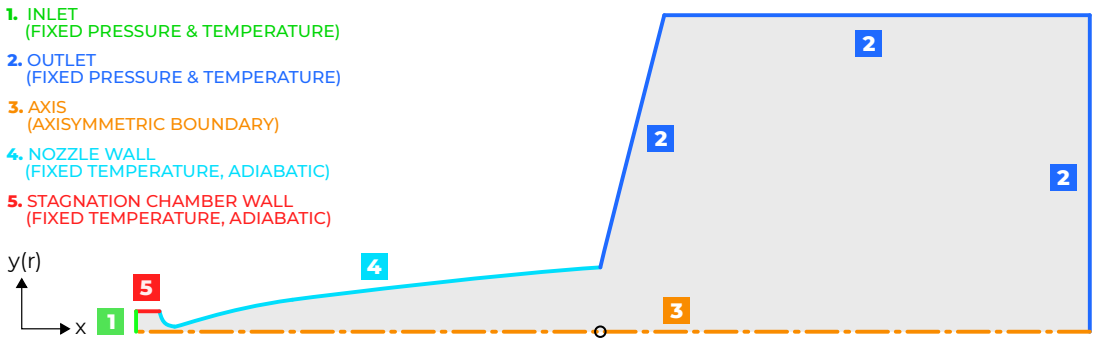

Figure 3. Diagram showing the boundary conditions set during CFD simulations of the LDT nozzle plume. All boundaries are shown to scale. The axes shown are aligned with the nozzle axes presented in Figure 2, with the origin being the centre of the nozzle exit (represented here by the black circle on the domain's lowermost boundary).

the characteristic length scale being considered (taken to be the probe diameter, $\varnothing$, in the present work).

The results of two radial Pitot surveys performed as part of the characterisation are presented in Figures 4 and 5, respectively. These data were sampled at $x = 100$mm and $x = 80$mm at mass flow rates of 10 and 25 SLPM, respectively (where $x = 0$ mm corresponds to the nozzle exit – see Figure 2), and are presented here as they validate the CFD simulations at locations proximate (or indeed, coincident, in the case of the survey performed at $x = 80$mm) to those selected for the transient thermal experiments. Figure 4 shows the Pitot pressure as measured by the traverse probe, while Figure 5 shows the ratio of Pitot and stagnation chamber (i.e. nozzle supply) pressures.

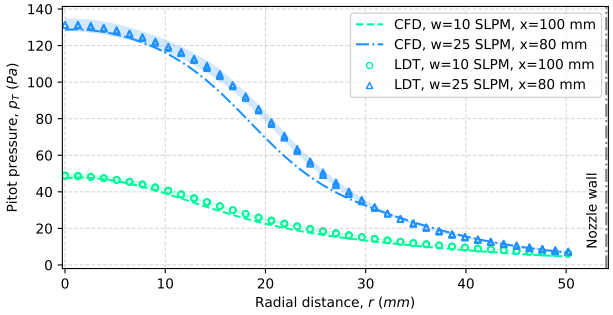

Figure 4. Plot of Pitot pressures downstream of the LDT nozzle exit at $x = 100$mm and $x = 80$mm. Results from CFD simulations at the same locations in the plume are also plotted. The shaded envelope indicates the measurement uncertainty for the experimental data.

Each data point corresponds to a single average over 5 seconds, with the probe held for 2 seconds at each location prior to recording in order to allow flow establishment, giving an overall experimental duration for a single survey of ~ 25 minutes. Five distinct surveys at each condition are plotted in Figures 4 and 5. The results lie on top of one another demonstrating that the facility control system, which comprises independent PID control loops for the LDT vapour booster, stagnation chamber heater, flow inline heater, and mass flow controller, has sufficient

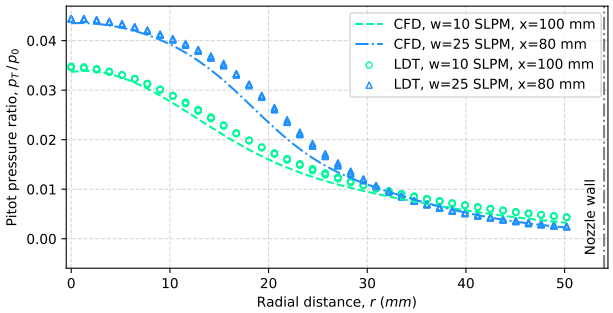

Figure 5. Plot of Pitot to stagnation chamber pressure ratio downstream of the LDT nozzle exit at $x = 100$ mm and $x = 80$ mm. Results from CFD simulations at the same locations in the plume are also plotted.

temporal stability over the duration of these experiments.

In the case of the Pitot pressure measurements presented in Figure 4, a shaded envelope is also plotted around these data to show the overall uncertainty of the pressure transducer(s) used to record the necessary measurements. Measurement uncertainties were calculated using the uncertainties specified by each individual sensors' manufacturer (see Table 1). The maximum uncertainties for any single measurement are 5.8% and 12.0% for the 10 and 25 SLPM conditions, respectively. The mean uncertainties (calculated over all measurements presented herein) are 3.2% and 3.7% for the 10 and 25 SLPM conditions, respectively.

Results of the accompanying CFD simulations of the LDT nozzle plume are plotted over the measurements. As previously mentioned, these data are included in order to demonstrate the validation of the CFD simulations against experimental data, and to support the use of interpolation of the CFD results in the design of the present work's experiments and DSMC simulations.

Note that although agreement between simulation and experiment is excellent near the centre of the flow (where radial distance, $r \to 0$), the thickness of the boundary layer towards the nozzle wall is slightly overpredicted in

Variable	Symbol	Unit	Condition 1	Condition 2
Mach number	Ma	–	5.79	5.39
Knudsen number	Kn	–	0.101	0.022
Total pressure	p_0	Pa	1231.2	2826.2
Total temperature	T_0	K	385	385
Static pressure	p_∞	Pa	0.97	2826.2
Static temperature	T_∞	K	50.3	56.7
Centreline Pitot pressure (exp.)	T_T	Pa	41.5	129.9
Probe diameter	$\varnothing$	m	0.01	0.015
Distance from nozzle exit	x	m	0.108	0.08
Mass flow rate	w	SLPM (g/s)	10 (0.198)	25 (0.494)

Table 3. LDT operating conditions for transient thermal experiments, as derived from interpolation of CFD simulations. The abbreviation "exp." indicates an interpolated value derived from experiments.

the higher mass flow rate case for $r > 10$ mm, with a commensurate disagreement also manifesting in the low mass flow rate case. This is due to the boundary conditions used in the CFD calculations, which do not account for surface roughness, variations in nozzle wall temperature, or the partial slip condition that is typically expected of slip regime flows.

Using the CFD results at $x = 0$, linear interpolation was used to extract the static properties of the flow downstream of the nozzle exit up to $x = 120$mm. The Knudsen number of the flow for each surveyed condition was then calculated using Equation 1, with a range of different values of characteristic length, L (which here is taken to be the same as the diameter of an experimental probe). The flow Knudsen numbers were found to increase monotonically with increasing distance from the nozzle exit. From these results, Knudsen numbers of 0.1 and 0.02 were selected for the present work's transient thermal experiments. These conditions were achieved at positions 108mm and 80mm downstream of the nozzle exit, with probe diameters of 10mm and 15mm, respectively. The inlet mass flow rates at which these conditions occurred were 10 and 25 SLPM, respectively.

The final set of selected variables for the two experimental flow conditions (which were calculated based upon the CFD simulations) are presented in Table 3. They are referred to as conditions 1 and 2 from here on.

3. EXPERIMENTAL SETUP

The transient thermal experiments performed during the present work utilised two hemisphere-cylinder probes of different diameters treated with a thermochromic liquid crystal (LC) slurry. Using a flow initialisation shield and remotely operated camera (a Panasonic DC-TZ90 recording MP4 H.264 video at 60 fps with a resolution of 1920 $\times$ 1080 pixels and an 8 bit colour depth), the transient heating of the probes in the hypersonic plume was monitored visually and the resulting colour changes in the LC coating recorded. These data were then post-processed using an in-house code developed at OTI, allowing surface distributions of heat transfer coefficient to be calculated.

The flow initialisation shield in the LDT test chamber was installed in order to allow an aluminium plate to be positioned in front of the nozzle using a stepper motor. This shield deflects the hypersonic plume around it, preventing it from interacting with a test piece situated behind it. The shield may be retracted at such a speed as to present a step change in flow conditions. Doing so prevents uneven heating of the probes which may otherwise be caused by translating them into the flow with a (comparatively) slow traversing mechanism or by initialising the plume using the mass flow controller to suddenly admit gas to the stagnation chamber. The former of these procedures would expose the probe to pre-heating in the low speed outer portions of the plume, while the latter would expose the probes to transient conditions during the initial formation of the plume, which are challenging to predict (as opposed to it being established and held at a steady state beforehand).

3.1. Hemisphere-cylinder probes

A pair of cylindrical probes with diameters of $\varnothing$10mm and $\varnothing$15mm with hemispherical tips were manufactured from Perspex and fixed in place along the centreline of the LDT's contoured nozzle. Each probe featured a $\varnothing$12mm section at the rear so that they could be mounted in the LDT test chamber using the same equipment, thereby reducing the need for angular realignments between tests. Diagrams of the probe geometries generated using CAD software are presented in Figure 6.

The diameter of each probe was selected based upon calculations of the Knudsen number, Kn in the LDT plume, which were themselves based upon interpolation of the CFD results presented in Section 2.

During LDT experiments, the probes were each allowed to thermally equilibrate in the test chamber for 2 hours.

This was done in order to mitigate the cooling effects caused by the initial depressurisation of the chamber once the probes had been installed. The initial temperature of each probe was measured using a K-type thermocouple affixed to the probe afterbodies (the unshaded sections with $\varnothing = 12\,mm$ shown in Figure 6) with polyamide (Kapton) tape.

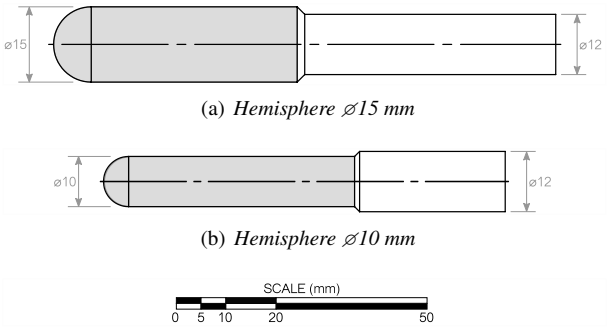

(a) *Hemisphere ⌀15 mm*

(b) *Hemisphere ⌀10 mm*

Figure 6. Schematic diagrams of experimental geometries. Shaded regions indicate surfaces which are treated with thermochromic liquid crystal slurries during manufacture.

3.2. Thermochromic liquid crystals

The heat transfer distribution was inferred in the present work through the use of thermochromic liquid crystals (LC) applied to each model. This method has been used extensively in previous studies at OTI, including those performed by Ryley [12], and Owen [11]. The methodology of utilising liquid crystals as a thermographic technique is described by Schultz and Jones [14], and later in much greater detail by Ireland and Jones [8], wherein their applicability to thermal flux experiments and strategies for post-processing the resultant data are described.

This measurement technique involves the application of a thermally thin LC layer to a substrate with known thermal properties. The chemical composition of the liquid crystals allows them to remain transparent both below and above their individual transition temperatures, which are determined during manufacture. A single LC coating (referred to as a slurry) may consist of multiple different LC formulations, thereby allowing it to exhibit multiple transition temperatures. When heated to their transition temperature, the crystals realign such that they rapidly cycle through red, green, and blue, before once again returning to transparency. As such, temperature changes may be tracked visually by recording the colour play (the variation in colour of the LC coating over time) over the surface of a model.

For the present work, liquid crystal coatings comprising three different LC slurries (with transition temperatures 25^oC, 30^oC, and 35^oC) were applied to test pieces using a pneumatic spray gun, and utilised a dark undercoat to improve the visual contrast of the colour play. Modern LC formulations like those used for the present work are often encapsulated in small polymer spheres of $\sim 50\mu m$ diameter which, as Ireland and Jones [8] report, renders them insensitive to pressure variations.

Figure 7 shows the final frame of one of the hemisphere probe tests wherein the LC coating was subjected to heating in the LDT nozzle plume.

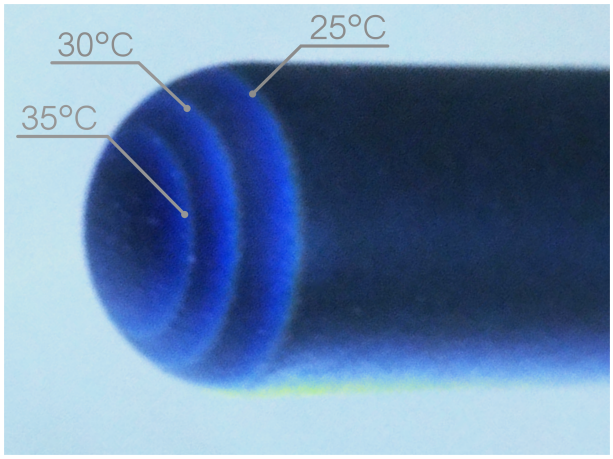

Figure 7. Photograph of the colour play on a test piece coated with a slurry comprising three encapsulated liquid crystal solutions with transition temperatures 25^oC, 30^oC, and 35^oC (labelled).

3.3. Calibration procedure

Although the transition temperature of a given LC slurry is stated by the manufacturer, mixtures of these solutions often have slightly different proportions of their constituent slurries. As such, a calibration procedure is required in order to define the expected visual response of an LC mixture to a variation in temperature.

The liquid crystal calibration procedure involves characterising the visible response of an LC mixture with respect to the surface temperature of the substrate to which it has been applied. These data can then be used as a lookup table to generate a simulated colour play with respect to a given thermal transient (i.e. a change in temperature over time). This is an essential part of the post-processing procedure, which is described further in Section 5.

To obtain these data, an LC solution was mixed thoroughly and applied to a thermally conductive substrate (a copper plate was utilised during the course of the present work) using a pneumatic paint sprayer in order to ensure an even coat. A K-type thermocouple was then applied to the upwards facing side of this calibration plate, and steady, even heating was performed while both the colour play and temperature of the calibration plate's surface were simultaneously recorded. In the case of the present work, a PID controlled, electrically heated hot plate was used as the heat source for calibration, and the colour play

was recorded using the same camera as the transient thermal experiments (see Section 3). This setup is pictured in Figure 8.

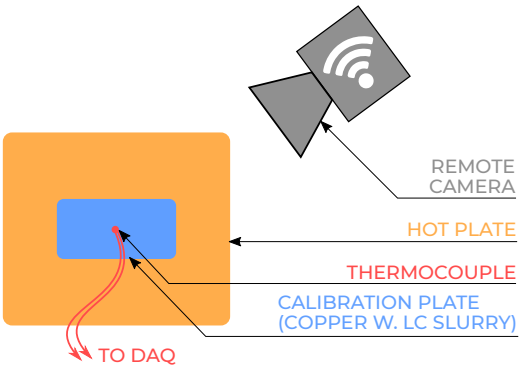

Figure 8. Liquid crystal calibration setup

Since LC slurries are mixed by technicians at OTI for individual experiments, there is an inherent variability of the slurry proportions in them. As such, it is vital to the calibration process that a mixture is applied to all calibration pieces and experimental probes simultaneously. This ensures that the same mixture (and, hence, the same proportions of the constituent slurries) is used both for experiments and calibration procedures.

The results of such a calibration are shown in Figure 10. The presented data were sampled from a 40 X 40 pixel window in the calibration video proximate to the thermocouple. The intensity of each colour channel of this video and the temperature recorded by the thermocouple are plotted against time. Data from the calibration video were subjected to Savitzky-Golay filtering [13] in order to mitigate channel noise. Note also that the standard uncertainty of a K-type thermocouple ($\pm 2.2\,K$ [1]) is also plotted as a shaded error envelope.

A lookup table is then generated for each colour channel with respect to the thermocouple temperature, allowing interpolation between a given temperature and the intensities of each colour channel. For the present work, the green channel was utilised exclusively as it was found that the red channel was too faint to analyse effectively and the large width of the blue channel transitions reduced the accuracy of the post-processing procedures. A photograph of a transient thermal experiment showing both the full-colour image and the separated green channel is presented in Figure 9.

4. DIRECT SIMULATION MONTE CARLO (DSMC) SIMULATIONS

Numerical predictions of the convective heat transfer coefficient, h_{conv}, were performed using Bird's DS2V code [2], a two-dimensional DSMC (Direct Simulation Monte Carlo) code. This tool was selected due to the high Knudsen numbers of the test conditions (see Table 3), which

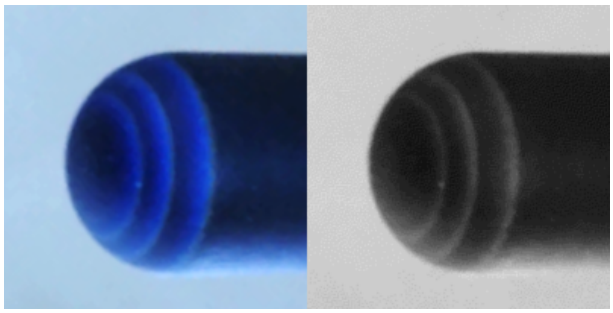

Figure 9. Stills of the experimental video showing the full colour image (left) and the separated green channel (right).

both lie in the slip-transition regime (where $0.001 \leqslant Kn \leqslant 1.0$).

For each condition in Table 3 two types of simulations were performed, each with a different wall boundary condition; one adiabatic, and one isothermal. The input conditions for DS2V were the wall temperature, which was set to $293\,K$ for the adiabatic cases, the gas species mass fractions, and the flow temperature, velocity, and number density. These data were derived from the CFD simulations described in Section 2, and are presented in Table 4.

From the results of these simulations, h_{conv} was calculated using Equation 2, where the initial wall temperature, T_{i}, was set to $293\,K$, the adiabatic wall temperature, T_{aw}, was derived from the adiabatic simulations, and the heat flux, $\dot{q}_{\text{conv}}$ was derived from the isothermal simulations.

In each simulation, an ideal gas comprising 21% O_2 and 79% N_2 was modelled. The rotational and vibrational energy accommodation coefficients were set to 1.0, as these temperature modes were expected to play a negligible role in heating compared to translational temperature. The surface specular reflection and adsorption factors were set to 0 owing to the lack of high enthalpies or significant radiative heating in the flow. Fully diffuse particle reflection with full accommodation to the surface temperature upon impact was assumed. No chemical reactions within the gas or at the model surface were modelled, once again due to the low total enthalpy of the flow produced in the LDT.

The grid used for each simulation was generated automatically by DS2V, and refined using a built-in subroutine once the flow had achieved a steady state (after ~ 100 sampling iterations). Several of the simulation parameters were also set automatically by the code. As such, the criteria for a "good" DSMC simulation as defined by Bird [3] were achieved. These criteria are listed below (note that λ is the local mean free path, as in Equation 1, and $\bar{t}$ is the mean free time, which is equal to the mean particle velocity divided by λ).

- Greater than 7 particles per sampling cell

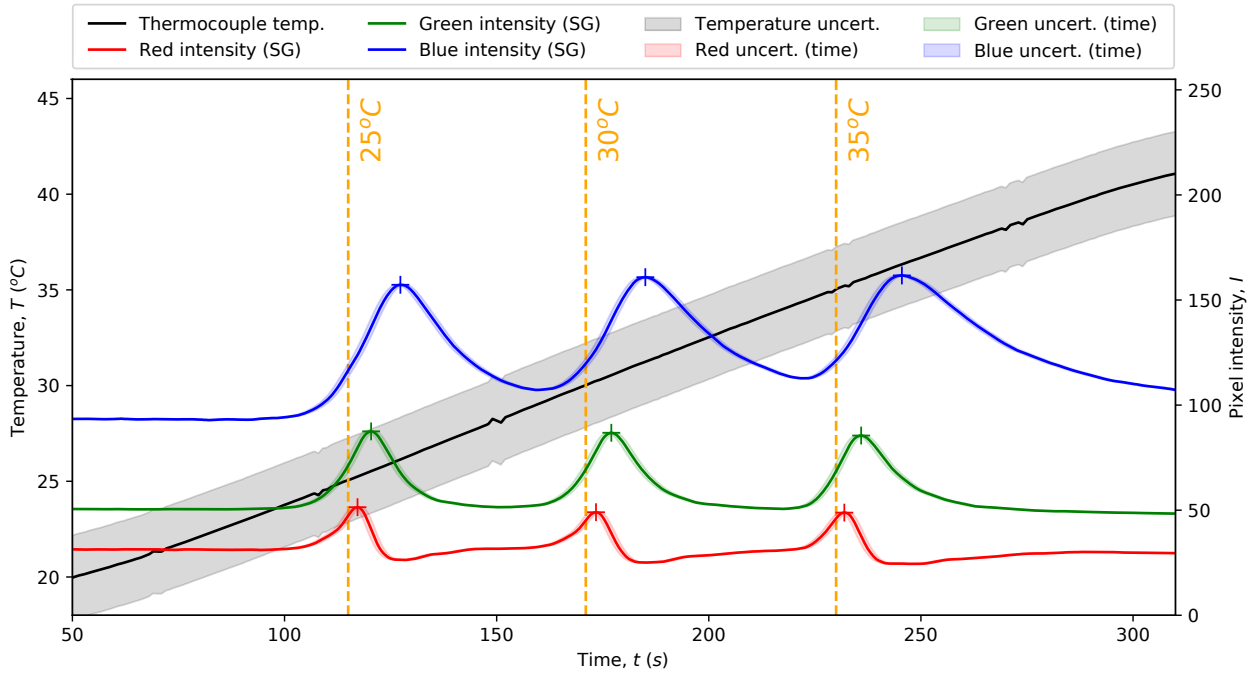

Figure 10. Liquid crystal calibration data measured during even heating of a copper plate. Video colour intensities and plate temperatures are plotted, and nominal transition temperature crossing times (at 25^oC, 30^oC, and 35^oC) are shown as dotted lines. The term "SG" refers to those data which have undergone Savitzky-Golay filtering.

Variable	Symbol	Unit	Condition 1	Condition 2
Freestream velocity	U_∞	m/s	822.75	813.53
Static temperature	T_∞	K	50.34	56.67
Species mass fractions	T_{aw}	$-$	$0.21\,O_2$, $0.79\,N_2$	$0.21\,O_2$, $0.79\,N_2$
Wall temperature	T_{aw}	K	293	293
Gas number density	n	m^{-3}	1.390×10^{21}	4.339×10^{21}

Table 4. Input variables for DS2V simulations.

- A collision cell size greater than $\lambda/3$
- A mean collision separation between particles greater than $\lambda/5$
- A time step smaller than $\bar{t}/3$

The thermal emissivity, ϵ, of the LC coatings is not well characterised, although it was expected to lie in the range $0.3 \leqslant \epsilon \leqslant 0.6$ (similar to the emissivities of unpolished metals) due to the dark undercoat and low optical specularity of the treated surfaces. In order to mitigate this uncertainty, a range of adiabatic DSMC simulations were performed where the surface ϵ value was varied in increments of 0.25 in the range $0 \leqslant \epsilon \leqslant 1$. The resulting adiabatic wall temperature data were then interrogated via 2D cubic interpolation during post processing in order to achieve the best match with experimental data. The same value of $\epsilon = 0.45$ was ultimately used to post process simulations for both flow conditions, since the coatings on both probes were assumed to be thermally identical (see Section 3.3.

$$h_{\text{conv}} = \frac{\dot{q}_{\text{conv}}}{T_{\text{aw}} - T_{\text{i}}} \tag{2}$$

5. ONE DIMENSIONAL TRANSIENT HEAT TRANSFER ANALYSIS

When studying thermal fluxes in a physical experiment, an ideal setup would include a step change in heat flux, $\dot{q}$, at the start of a test, where said heat flux then remains constant throughout. For such an experiment, the resulting changes in temperature are easily analysed to determine the thermal response of the test piece. In high Mach number flow experiments, however, it is often challenging to generate a perfect step of $\dot{q}$, especially in low enthalpy, long duration facilities such as the LDT. Instead, a step change in flow temperature is often sought, whereby the model under test is heated asymptotically towards the recovery temperature of the gas, T_{r}. The expression for

T_r in a supersonic flow is presented in Equation 3. This strategy naturally causes heat flux to decrease from an initially high value as the temperature of a test piece's substrate material increases from its initial temperature, T_i, towards T_r. The convective heat transfer coefficient, h_{conv}, is the output of this kind of study as, by definition, it remains time invariant provided the test flow conditions remain steady.

$$T_r = T_\infty \left(1 + r\frac{\gamma - 1}{2} {Ma_\infty}^2\right) \tag{3}$$

Schultz and Jones [14] described this technique in detail, describing the analytic rise in temperature at the surface of a model with Equation 5 where the variable β is given by Equation 4. Note that the variables ρ, C, and k are the density, specific heat capacity and conductivity of the substrate material. The square root of the product of these variables, $\sqrt{\rho C K}$ is referred to as the "thermal product", and is often taken as a single unified measure during thermal analyses. For Perspex, both this value and its uncertainties have been quantified by Ireland [9] to be $569 \pm 29\ J{\cdot}s^{-0.5}{\cdot}K^{-1}{\cdot}m^{-2}$. With the assumption of semi-infinite conduction, the rise in model surface temperature for a step change in flow temperature is described by Equations 4 and 5.

$$\beta = \frac{h_{conv}\sqrt{t}}{\sqrt{\rho C k}} \tag{4}$$

$$\theta = \frac{T_s - T_i}{T_r - T_i} = 1 - e^{\beta^2}\,\mathrm{erfc}\,(\beta) \tag{5}$$

This model assumes that the thermal fluxes within the model substrate behave such that it may be considered semi-infinite in all directions except depth, i.e. the vast majority of heat transfer occurs normal to the probe surface. In the case of an initially cold body in a heated flow (of constant temperature), this assumption has only a limited time during which it may be considered valid. This time is characterised by Equation 6, where x_{tp} is the depth to which a thermal pulse penetrates a semi-infinite substrate in a time, t_{tp}, and α is the thermal diffusivity of the substrate material (Equation 7).

$$t_{tp} = \frac{x_{tp}^2}{4\alpha} \tag{6}$$

$$\alpha = \frac{k}{\rho c} \tag{7}$$

Analysing transient heat transfer in this fashion is an extremely efficient method for calculating h_{conv}, as it relies solely upon Equations 5 and 4.

Referring to Equation 6, it may be observed that the time at which a thermal pulse begins to interact with itself near the centre of some medium with thermal diffusivity, α, is t_{tp}. If the dimensions of an experimental test piece are approximately comparable in all directions, Equation 6 (with x_{tp} set to the smallest of these dimensions), may be used to calculate the allowable test duration. Beyond this time, the semi-infinite substrate assumption will be invalidated.

In the case of the hemispherical probes used for the present work, x_{tp} was set to the radius of each test piece, i.e. $\varnothing/2$. giving periods of validity for the semi-infinite assumption of 25s and 11s for probes 1 and 2, respectively. As such, these times represent the point in an experiment after which the semi-infinite substrate assumption becomes invalid, and hence, the point up to which one-dimension thermal analyses may be performed.

The tool used for one dimensional analysis of the hemisphere cases is called THTAC (Transient Heat Transfer Analysis Code) [15], and is an in-house code developed at OTI using Matlab. Using equations 5 and 4, THTAC calculates the transient temperature rise for a range of user-specified values of h_{conv}. The liquid crystal calibration lookup table is then used to generate a simulated intensity profile for each specified value of h_{conv}, and these are compared to the actual values from the experimental video. Once comparisons of experimental and simulated intensities have been made, the value of h_{conv} which produced the lowest error between the two series is selected as that pixel's value.

6. RESULTS AND DISCUSSION

The results of the DSMC simulations and transient heat transfer experiments performed in the LDT are presented in this section. The simulation results are discussed briefly before subsequently being compared to the experimental results.

6.1. DSMC simulations

The DSMC simulations modelled the surface heat transfer coefficients by simulating the hypersonic flowfield surrounding the hemisphere models. The results of the flowfield simulations for the isothermal cases are presented in Figure 11.

It is clear that the simulation performed at condition 1, which featured a high freestream Knudsen number of $Kn = 0.1$, exhibits a thicker boundary layer and a far more diffuse shock than that of the simulation for condition 2 (whose Knudsen number was 0.02, approximately one order of magnitude lower). This was expected to result in lower heat fluxes across the surface of the hemisphere probes for condition 1, with a "flatter" distribution also being exhibited due to the higher level of rarefaction.

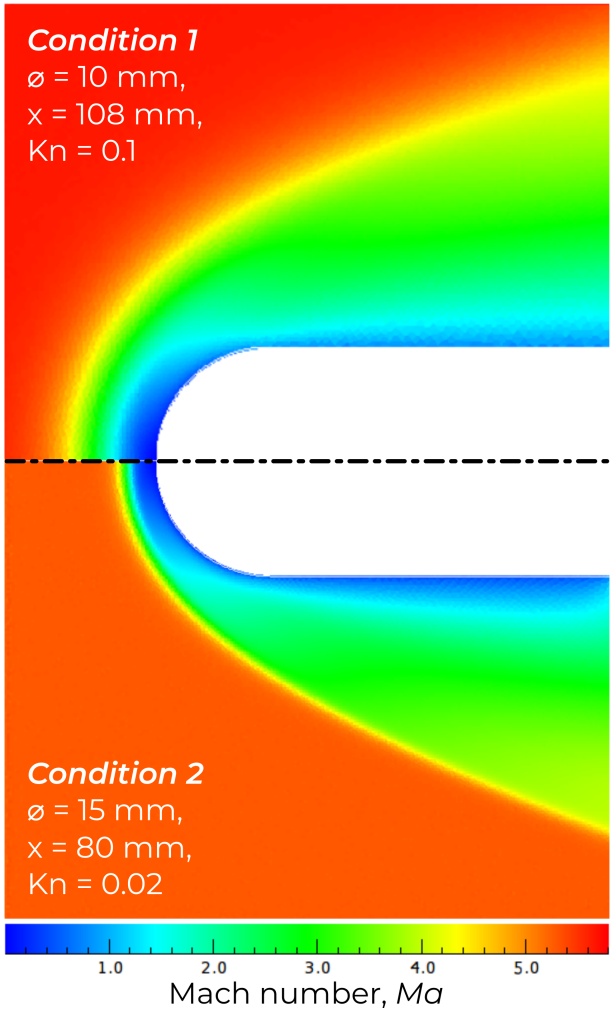

Figure 11. Contours of Mach number for two hemispheres in low density hypersonic flow simulated using DS2V. The upper figure shows the ⌀10mm probe at condition 1, while the lower figure shows the ⌀15mm probe at condition 2. The geometric scale of each simulation has been normalised to better compare the flow structures.

6.2. Experimental results

Contour plots of the convective surface heat transfer coefficient, h_{conv}, as calculated by THTAC are presented in Figures 12 and 13 for conditions 1 and 2, respectively. The derived distributions of h_{conv} are extremely smooth across both cases, with few asymmetric or erroneous features.

Regions with a seemingly random distribution of h_{conv} are the result of there being no LC colour play data for THTAC to analyse, resulting in essentially random fitting by the code. The small region of low h_{conv} visible near the stagnation point of each hemisphere probe are the result of small specular reflections on the probes, which were in turn caused by uneven lighting in the LDT test chamber. These reflections caused the pixel intensities in these locations to become saturated, thereby disrupting THTAC's ability to analyse the colour play on the probe surfaces. As such, both of these features may be considered erroneous, and may be disregarded when considering the solutions.

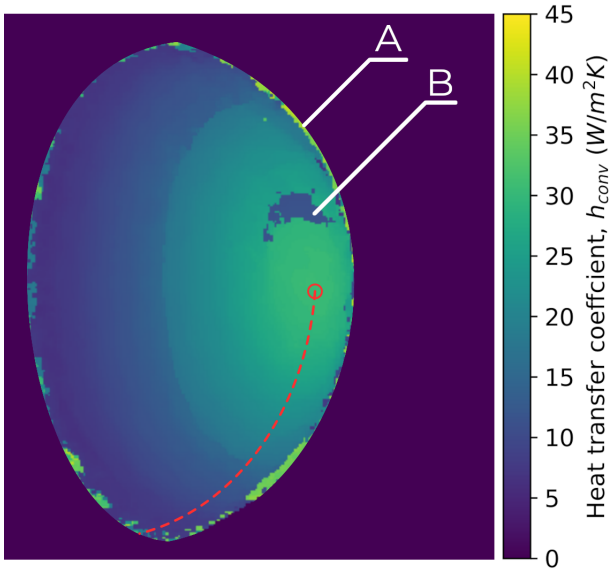

Figure 12. Contours of HTC generated using THTAC from experiments conducted at condition 1 using the ⌀10mm probe. The sampling line used for data extraction and stagnation point location are indicated by the dashed curve and circle, respectively.

As expected, the magnitude of the h_{conv} results at condition 2 are lower than those at condition 1. This is due to the higher degree of flow rarefaction in condition 1 (previously observed in Figure 11), resulting in fewer particulate collisions with the test probe and, hence, a lower overall transfer of thermal energy to the surface.

It is also evident that results from the condition 2 case feature a slightly larger area of good quality, non-random data than those run at condition 1. This is the result of a lower overall change in temperature over the course of the test at condition 1, an effect which is caused by two main factors. The first is the difference in allowable test time between cases (described in Section 5), which necessitated the duration of the test run at condition 1 being less than half that of the test run at condition 2. The second is simply the aforementioned difference in heat flux between the two experiments, which was expected to be larger for the condition 2 results.

Both the simulated and experiment-derived data are presented here in Figures 14 and 15 for conditions 1 and 2, respectively. These data were extracted from the wall boundary in the case of the DSMC simulations, and by defining a curve comprising discrete interpolation points in the case of the experimental data. In the latter of these cases, the sampling arc was translated such that its end was coincident with the probe stagnation point for each set of results, and was then rotated using Euler matrices

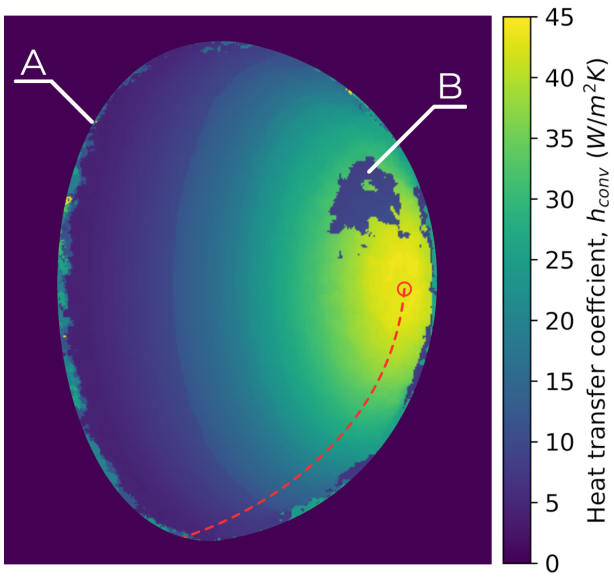

Figure 13. Contours of HTC generated using THTAC from experiments conducted at condition 2 using the ⌀15mm probe. The sampling line used for data extraction and stagnation point location are indicated by the dashed curve and circle, respectively.

to match the orientation of the test probes relative to the camera. These sampling series are denoted by red dashed arcs in Figures 12 and 13, with the stagnation points being denoted by circular markers.

In order to compare results from both probes, normalised arc lengths were calculated by dividing the length of each sampling arc by $\pi R_{\mathrm{n}}/2$ (where R_{n} is the nose radius of each probe). As such, $2x/\pi R_{\mathrm{n}} = 0$ (where x is the arc length) corresponds with the stagnation point for each probe, and $2x/\pi R_{\mathrm{n}} = 1$ with the tangent point between the hemispherical and cylindrical sections of the geometries.

The error envelop that is included in each plot was generated using an uncertainty calculator built in to THTAC. This tool allows the initial conditions of the experimental data to be perturbed such that the effects of variances in their values upon the final h_{conv} distributions may be determined. These variation and their contributions to the experimental uncertainty are shown in Table 3. The overall root-sum-square (RSS) uncertainties plotted in Figures 14 and 15 were calculated using Equation 8.

$$\epsilon_{RSS} = \sqrt{\sum_{i=1}^{N} \epsilon^2} = \sqrt{\sum_{i=1}^{N} \left(y_i - f(x_i)\right)^2} \qquad (8)$$

The largest source of uncertainty at the stagnation point of the hemisphere is the probe's initial temperature, T_{i}, which was perturbed by $\pm 2.2\,K$ – the uncertainty of K type thermocouples, as was used to measure each model's

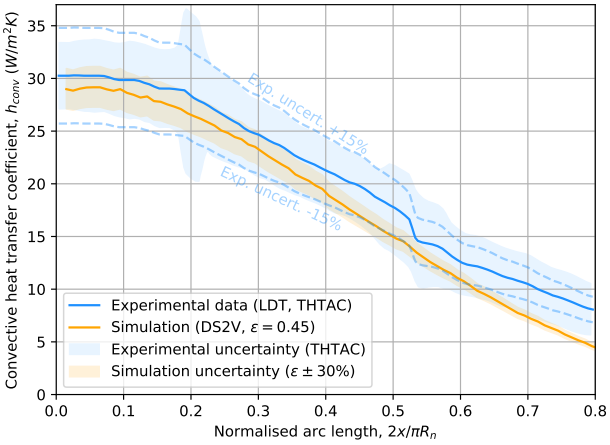

Figure 14. Plot of experimental and simulated h_{conv} over the ⌀10mm hemisphere probe at condition 1. Uncertainties are indicated by shaded envelopes, and a nominal $\pm 15\%$ experimental uncertainty is indicated by the dotted lines.

initial temperature – during uncertainty quantification. This resulted in uncertainties of 18.3% and 14.1% for conditions 1 and 2, respectively. The next greatest source is the temporal offset of the experimental video, which is assumed to coincide with the start of heating in an experiment. This variable was perturbed by $\pm 1\,s$ and resulted in uncertainties of 6.9% and 8.3% for conditions 1 and 2, respectively. This is followed by variation in the thermal product of the probe substrates, $\sqrt{\rho\,C\,k}$, which was perturbed by $\pm 29\,J{\cdot}s^{-0.5}{\cdot}K^{-1}{\cdot}m^{-2}$, an uncertainty value determined by Ireland [9]. The experimental uncertainty caused by this variation is 5.5% and 4.8% for conditions 1 and 2, respectively. The uncertainties at the hemisphere stagnation points are summarised in Table 5.

Variations in the liquid crystal calibration temperatures, gas temperature rise time, and h_{conv} discretisation introduce far smaller uncertainties than the other contributors, at 2.7%, 2.1%, and 0.7% (respectively) for condition 1, and 2.0%, 2.0%, and 0.7% for condition 2.

It is clear from these data that the largest sources of uncertainty are the probes' initial temperatures, the starting times of experimental videos, and the material of which the probes are constructed.

Additionally, the flow shield mentioned in Section 2 (which is responsible for blocking the hypersonic plume, hence preventing it from interacting with the probes prior to the start of an experimental run) is visible at the beginning of each of the experimental videos, and so could be observed on a frame-by-frame basis during its transit out of the flow. This, coupled with the experimental recording frame rate of 60 FPS, allowed the start time of each experiment to be measured relatively accurately. The perturbation value of $\pm 1\,s$, then, may be considered somewhat conservative.

Considering Figure 14, it may be observed that the condition 1 case shows good agreement in terms of abso-

Parameter	Variation	Contribution to h_{conv} uncertainty	
		Condition 1	Condition 2
Initial temperature	$\pm 2\,K$	18.3%	14.1%
Video start time offset	$\pm 1\,s$	6.9%	8.3%
Thermal product (Perspex)	$\pm 29\,J{\cdot}s^{-0.5}{\cdot}K^{-1}{\cdot}m^{-2}$	5.5%	4.8%
LC calibration temperatures	$\pm 0.25\,K$	2.7%	2.0%
Gas temperature rise time	$\pm 2\%$	2.1%	2.0%
h_{conv} discretisation error	–	0.7%	0.7%
Overall RSS uncertainty	–	20.6%	17.3%

Table 5. Contributions to experimental uncertainty at the stagnation point of the hemispherical probes.

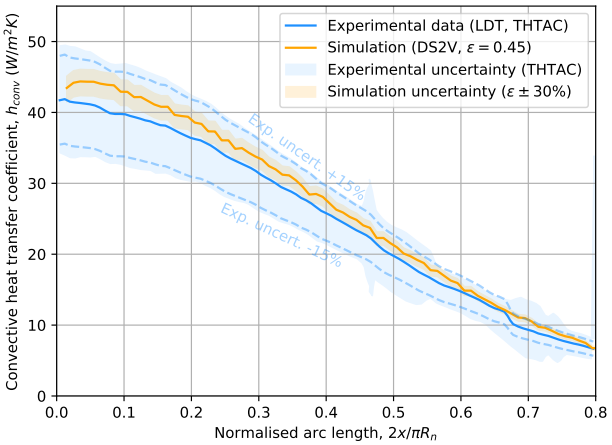

Figure 15. Plot of experimental and simulated h_{conv} over the ⌀15mm hemisphere probe at condition 2. Uncertainties are indicated by shaded envelopes, and a nominal $\pm 15\%$ experimental uncertainty is indicated by the dotted lines.

lute h_{conv} values, with a relative error of 4.5% near the stagnation point, and errors which steadily increase as $2x/\pi R_n \rightarrow 0.8$. A maximum error of $\sim 41.8\%$ was calculated towards the probe's cylindrical section (where $2x/\pi R_n = 0.8$). It should be noted, however, that the absolute error between experimental and simulated values here is only $3.5\,W{\cdot}m^{-2}{\cdot}K^{-1}$.

As is apparent from Figure 15, the results from the condition 2 case show similarly good agreement between simulated and experimental h_{conv} measurements. The maximum percentage error between the simulated and experimental h_{conv} is $\sim 13.0\%$ at $2x/\pi R_n \approx 0.7$, and approaches zero as $2x/\pi R_n \rightarrow 0.8$. The error at the stagnation point was 5.3%

It may be concluded from these cases that the LDT experimental results produce excellent overall agreement with DSMC simulations run using *DS2V* for hemispheres at Knudsen numbers in the slip and lower transition regimes.

7. CONCLUSION

In this paper, a pair of transient thermal experiments were described, and their results presented.

A characterisation study of the Low Density Tunnel (LDT), an experimental facility designed to study hypersonic aerothermodynamics, has also been presented. This study has demonstrated the suitability of the tunnel for the study of space debris demise. It was also used in conjunction with CFD simulations to identify two experimental conditions used for the present work. Both conditions exhibited hypersonic Mach numbers in excess of $Ma = 5$ and Knudsen numbers in the slip-transition regime $0.001 \leqslant Kn \leqslant 1.0$.

An existing thermodynamic experimental technique featuring thermochromic liquid crystals was utilised to measure the temperature change over the surface of two hemisphere-cylinders. An in-house code developed at OTI was then used to postprocess the resulting videos, resulting in high quality convective heat transfer coefficient data. When compared to data extracted from DSMC simulations, these data were found to exhibit excellent agreement with a maximum error of 5.3% at the probe stagnation points, and a maximum experimental uncertainty of 18% at the same location.

ACKNOWLEDGMENTS

This research was funded by grants from the UK Science and Technology Facilities Council (STFC) and the Engineering and Physical Science Research Council (EPSRC) via the National Wind Tunnel Facility programme (NWTF). Additional funding was supplied by Fluid Gravity Engineering (FGE).

REFERENCES

1. R. L. Anderson, "Thermocouple Error Analysis in the Design of Large Engineering Experiments," p. 51, 1979.

2. G. A. Bird, *Molecular gas dynamics and the direct simulation of gas flows*. Oxford: Clarendon Press, 1994.
3. Bird, G, *The DSMC Method*, 1.2. 2013, ISBN: 9781492112907.
4. G. Dahlen, "Cone Drag in the Transition from Contiuum to Free Molecular Flow," England, UK, Tech. Rep., 1984.
5. N. L. Donaldson *et al.*, "Refurbishment and Characterisation of the Oxford Low Density Hypersonic Wind Tunnel," in *Proceedings of the International Conference on Flight Vehicles, Aerothermodynamics, and Re-Entry Missions & Engineering*, Monopoli, Italy, 2019.
6. N. L. Donaldson, "Hypersonic Modelling and Testing of Space Debris During Planetary Entry," Ph.D. dissertation, University of Oxford, 2019.
7. T. F. Haslam-Jones, "Measurements of the drag of slender cones in hypersonic flow at low Renolds numbers using a magnetic suspension and balance.," Thesis, 1977.
8. P. T. Ireland and T. V. Jones, "Liquid crystal measurements of heat transfer and surface shear stress," *Measurement Science and Technology*, vol. 11, no. 7, Jan. 2000.
9. P. Ireland, "Internal Cooling of Turbine Blades," Ph.D. dissertation, University of Oxford, 1987.
10. *Molecular sizes*. Encyclopedia Britannica, 2020.
11. A. Owen, "Experimental Studies of the Hypersonic, Low Density, Aerodynamics of Re-entry Vehicles," Ph.D. dissertation, Oxford, UK, 1997.
12. J. Ryley, "Turbine Blade Mid-Chord Internal Cooling," Thesis, University of Oxford, 2014.
13. A. Savitzky and M. J. E. Golay, "Smoothing and Differentiation of Data by Simplified Least Squares Procedures.," *Analytical Chemistry*, vol. 36, no. 8, pp. 1627–1639, Jul. 1964, ISSN: 0003-2700. DOI: 10.1021/ac60214a047.
14. D. L. Schultz and T. V. Jones, "Heat-Transfer Measurements in Short-Duration Hypersonic Facilities," English, Oxford, UK, Tech. Rep., 1973.
15. B. Tang, M. McGilvray, and D. Gillespie, *Transient Heat Transfer Analysis Code (THTAC) Instructions for End Users*, Osney Thermofluids Institute, University of Oxford, 2018.
16. C. F. Wilson, "Measurement of wind on the surface of Mars," English, Ph.D. dissertation, Oxford, UK, 2003, p. 150.